# Energy-resolved coherent diffraction from laser-driven electronic motion in atoms

Hua-Chieh Shao and Anthony F. Starace

Phys. Rev. A **96**, 042706 — Published 12 October 2017

DOI: 10.1103/PhysRevA.96.042706

# Energy-resolved coherent diffraction from laser-driven electronic motion in atoms

Hua-Chieh Shao* and Anthony F. Starace†
*Department of Physics and Astronomy, The University of Nebraska, Lincoln, Nebraska 68588-0299, USA*
(Dated: September 25, 2017)

We investigate theoretically the use of energy-resolved ultrafast electron diffraction to image laser-driven electronic motion in atoms. A chirped laser pulse is used to transfer the valence electron of the lithium atom from the ground state to the first excited state. During this process the electronic motion is imaged by 100-fs and 1-fs electron pulses in energy-resolved diffraction measurements. Simulations show that the angle-resolved spectra reveal the time evolution of the energy content and symmetry of the electronic state. The time-dependent diffraction patterns are further interpreted in terms of the momentum transfer. For the case of incident 1-fs electron pulses, the rapid $2s$-$2p$ quantum beat motion of the target electron is imaged as a time-dependent asymmetric oscillation of the diffraction pattern.

## I. INTRODUCTION

Coherent diffraction imaging is a technique that uses the wave property of incident probe particles (such as electrons and photons) to image microscopic target structures by diffraction [1–4]. Due to their (sub-)ångström wavelengths, ultrafast electrons and x rays have long been employed to determine the structures of atoms, molecules, crystals, and proteins [5–7]. Recent technological advances have dramatically reduced the duration and/or enhanced the brightness of the incident probe pulses [8–11]. As a result, such observation of atomic motions in reactions is enabling investigation of reaction dynamics [12]. In particular, ultrafast electron techniques such as electron diffraction, crystallography, and microscopy provide effective table-top instruments to study reaction mechanisms in various systems [13–17]. Gas-phase ultrafast electron diffraction has been used to probe transient structures during photoinduced chemical reactions [18], to study alignment, deformation, and ionization of carbon disulfide in a strong laser pulse [19], and to observe the oscillation and spread of an excited molecular wave packet of iodine [20]. In crystalline systems, particular reaction modes participating in molecular motions involving charge transfers have been identified in laser-induced phase transitions of molecular crystals [21, 22]. Structural changes in phase transitions such as liquid to crystal of $TiO_2$ [23], semiconductor to metal of $VO_2$ [24], and amorphization of $Ge_2Sb_2Te_5$ [25] have been reported. Oscillating electromagnetic waveforms in metamaterial resonators have been measured by ultrafast electron microscopy [26].

While these experiments on photoinduced reactions have unveiled underlying mechanisms, the roles played by electrons in these processes must still be inferred owing to current inability to resolve the electronic motions. The electronic motions initiate the atomic and molecular motions in these reactions, and the interplay between the electronic and nuclear degrees of freedom governs the ensuing reaction paths. Observing electronic motions can thus better relate structures to dynamics and, accordingly, provide a deeper understanding of the reaction dynamics. Nowadays femtosecond (fs) electron pulses with energies from tens of keV to MeV have been produced [27–31]. Recently, Maxson *et al.* compressed relativistic electron pulses to sub-10-fs bunch lengths [32]. Furthermore, various schemes to generate attosecond electron pulses have been proposed [33–38]. Simulations have demonstrated the possibility of imaging electronic motions in atoms and molecules by coherent diffraction imaging [39–44].

Owing to these promising developments, we have proposed the imaging of a laser-driven electronic motion in lithium atoms by ultrafast electron diffraction under feasible experimental conditions [45]. A chirped laser pulse adiabatically transfers the valence electron of the lithium atom from its $2s$ ground state to its $2p$ excited state on a picosecond (ps) time scale [46, 47]. During this process fs electron pulses are scattered from the atoms, rendering time-dependent diffraction images. Our previous results show the capability of electron pulses to image such an electronic population transfer. However, owing to the presence of the pump laser, the energy content of the lithium atoms is constantly changing. Without energy-resolved measurements, this important information is lost. By mapping the energy changes of the electrons during a reaction, one obtains valuable insights for understanding the reaction mechanisms. Energy-resolved coherent diffraction imaging has been simulated both for electron and x-ray pulses [43, 48], but the wave functions of the targets were assumed to be coherent superposition states whose average energies are constant. In contrast, in this work we study energy-resolved ultrafast electron diffraction from laser-driven population transfer in lithium atoms (Fig. 1). We investigate how the electronic motion and its energy content are reflected in the energy-resolved diffraction patterns. Simulations are presented for two pulse durations, and the diffraction patterns are interpreted in terms of the momentum transfers.

The paper is organized as follows: In Sec. II we

* E-mail: hcshao@huskers.unl.edu
† E-mail: astarace1@unl.edu

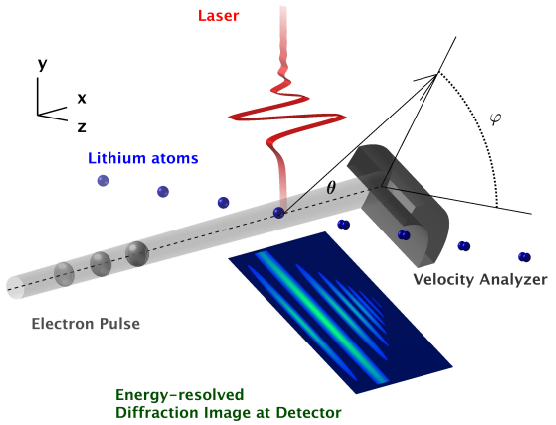


FIG. 1. (Color online) Schematic setup for energy-resolved ultrafast electron diffraction from a laser-driven electronic motion in lithium atoms. The valence electrons of the lithium atoms are adiabatically transferred from the $2s$ to $2p$ states by a chirped laser pulse. During the population transfer, ultrafast electron pulses collide with the atoms. Then energies of the scattered electrons are determined by the velocity analyzer, and the detector records the angle-resolved spectrum of the scattered electrons. Diffraction patterns as functions of scattering angles $\theta$ and $\varphi$ can be obtained by rotating the velocity analyzer. By varying the pump-probe delay time, the time- and energy-resolved diffraction images exhibit the spatial and energy details of the electronic motion. For future reference, the scattering angles $\theta$ and $\varphi$ and the coordinates system are defined here.

present a general theory for modeling ultrafast electron diffraction from a laser-driven system. The details of implementing the theory in our simulations are given in Sec. III. We then present and discuss our results, the energy-resolved diffraction images of the population transfer, in Sec. IV. Finally, we summarize our results and present our conclusions in Sec. V.

## II. THEORY

Conventional theories used to describe laser-assisted electron-atom collisions [49–51] are inadequate for imaging population transfer. First, the laser fields are frequently treated as plane waves, whereas in population transfer the pump laser pulses have finite durations, tailored pulse profiles, and/or chirps. Second, the atoms are usually modeled as potentials, thus lacking internal structures, or represented as a single Floquet state (which is a steady state), whereas population transfer involves transitions among several target states. For these reasons, we develop here a scattering theory to properly model the scattering from a laser-driven system. The theory is presented in a general context in this section, and further approximations specific to our system are discussed in the next section. Atomic units (a.u.) are used throughout the paper unless specified otherwise.

### A. Scattering from a laser-driven system

Consider a *scattering system* in which a projectile electron with momentum $\boldsymbol{k}_0$ collides with an atomic target $A$ with momentum $\boldsymbol{k}_1$:

$$e^-(\boldsymbol{k}_0) + A^*(\boldsymbol{k}_1) \to e^-(\boldsymbol{k}_a) + A^*(\boldsymbol{k}_b)\,, \tag{1}$$

where $\boldsymbol{k}_a$ and $\boldsymbol{k}_b$ are respectively the momenta of the electron and target after the collision. This scattering system is assumed to be influenced by an external laser pulse that induces a population transfer between the electronic states of the target. During this pump process, the time-varying electronic transitions are imaged by the scattered incident electron pulse.

The Hamiltonian for the scattering system and its interaction with the laser field is

$$H(t) = H_0 + H_1 + V(t)\,, \tag{2}$$

where $H_0$ and $H_1$ are the respective Hamiltonians of the projectile electron and target. The interaction potential $V(t)$ comprises two parts:

$$V(t) = V_\alpha(t) + V_\beta\,, \tag{3}$$

where $V_\alpha(t)$ is the time-dependent interaction of the scattering system with the laser pulse, and $V_\beta$ is the interaction between the electron and target. The dipole approximation is assumed for $V_\alpha(t)$, so the magnetic component of the laser field and the spatial dependence of the electric field are neglected. If the length gauge is used, one has

$$V_\alpha(t) = -\boldsymbol{d}\cdot\boldsymbol{E}(t)\,, \tag{4}$$

where $\boldsymbol{d}$ is the dipole operator of the scattering system and $\boldsymbol{E}(t)$ is the electric amplitude of the laser field.

Let $\psi_i$ be the eigenstate of $H_0 + H_1$ corresponding to the initial condition of the pump process, and let $\psi_f$ be the eigenstate of an exit channel. We assume that these asymptotic states exist for the interaction $V(t)$ as $t \to \pm\infty$, that the duration of the laser pulse is finite, and that $V_\beta$ is well behaved. The transition amplitude from the initial state $i$ to the final state $f$ can be calculated from the $S$ matrix [52, 53]:

$$S_{fi} = \delta_{fi} - i\int_{-\infty}^{\infty} dt\,\left(\psi_f(t), V(t)\,\psi_i^{(+)}(t)\right)\,, \tag{5}$$

where $\delta_{fi}$ is the Kronecker $\delta$ function, and $\psi_i^{(+)}(t)$ is a solution of the Schrödinger equation for the full Hamiltonian $H(t)$, with the outgoing-wave boundary condition denoted by the superscript $(+)$.

### B. Time-dependent distorted-wave approximation

In ultrafast electron diffraction $V_\beta$ is expected to be treated as a perturbation owing to the high collision energies [55]. Since $V(t)$ involves two types of interactions,

$V_\alpha(t)$ and $V_\beta$, it is useful to reformulate the scattering amplitude as a distorted-wave approximation in which the "distortion" of the wave function by $V_\alpha(t)$ is fully accounted for, while $V_\beta$ is treated perturbatively to correct the distorted wave due to the collision. In order to rewrite the $S$ matrix, we introduce the exact solution $\psi^{(-)}_{\alpha f}(t)$ of the following Schrödinger equation:

$$i\frac{\partial\psi^{(-)}_{\alpha f}(t)}{\partial t} = \big(H_0 + H_1 + V_\alpha(t)\big)\,\psi^{(-)}_{\alpha f}(t)\,. \tag{6}$$

The subscript $\alpha$ denotes that $\psi^{(-)}_{\alpha f}(t)$ is a solution under the laser interaction $V_\alpha(t)$, and the subscript $f$ indicates that $\psi^{(-)}_{\alpha f}(t)$ satisfies the asymptotic condition:

$$\psi^{(-)}_{\alpha f}(t) \to \psi_f(t) \quad \text{as} \quad t\to\infty\,. \tag{7}$$

We define $\psi^{(-)}_{\alpha f}(t)$ as the solution of the integral equation:

$$\psi^{(-)}_{\alpha f}(t) = \psi_f(t) + \int dt'\, G^{(-)}(t-t')\,V_\alpha(t')\,\psi^{(-)}_{\alpha f}(t')\,, \tag{8}$$

where $G^{(-)}(t)$ is the advanced Green's function of $H_0+H_1$. One has a similar equation for $\psi^{(+)}_i(t)$:

$$\psi^{(+)}_i(t) = \psi_i(t) + \int dt'\, G^{(+)}(t-t')\,V(t')\,\psi^{(+)}_i(t')\,, \tag{9}$$

where $G^{(+)}(t)$ is the retarded Green's function. Substituting $\psi_f(t)$ from Eq. (8) and $V(t)$ from Eq. (3) into Eq. (5) and using $G^{(-)\dagger}(t) = G^{(+)}(-t)$ and $\psi^{(+)}_i(t) - \psi_i(t)$ from Eq. (9), one can rewrite the $S$ matrix as:

$$\begin{aligned} S_{fi} = \delta_{fi} &- i\int dt\,\Big(\psi^{(-)}_{\alpha f}(t), V_\alpha(t)\,\psi_i(t)\Big) \\ &- i\int dt\,\Big(\psi^{(-)}_{\alpha f}(t), V_\beta\,\psi^{(+)}_i(t)\Big)\,. \end{aligned} \tag{10}$$

This expression is suitable for pump-probe processes since the respective interactions $V_\alpha(t)$ and $V_\beta$ are separated, which is useful for perturbative approximations. The second term on the right-hand side describes the transition from the initial state $\psi_i$ to the final state $\psi_f$ induced by the laser interaction $V_\alpha(t)$ alone, *i.e.,* this term depicts only the laser-driven population transfer in the target and the dressing of the wave function of the projectile electron. The last term describes the scattering process in which the projectile-target interaction $V_\beta$ induces the transition from the exact wave function $\psi^{(+)}_i(t)$ to the final state $\psi_f$. Since we are concerned with the time-resolved diffraction of the scattered electrons, the transition amplitude of interest is defined by the last term:

$$\mathscr{T}_{fi} \equiv \int dt\,\Big(\psi^{(-)}_{\alpha f}(t), V_\beta\,\psi^{(+)}_i(t)\Big)\,. \tag{11}$$

In the first-order Born approximation, the effect of $V_\beta$ on $\psi^{(+)}_i(t)$ can be neglected, so $\psi^{(+)}_i(t)$ can be approximated by the wave function that takes only $V_\alpha(t)$ into account:

$$\psi^{(+)}_i(t) \simeq \psi^{(+)}_{\alpha i}(t)\,, \tag{12}$$

where $\psi^{(+)}_{\alpha i}(t)$ satisfies the initial condition:

$$\psi^{(+)}_{\alpha i}(t) \to \psi_i(t) \quad \text{as} \quad t\to-\infty\,. \tag{13}$$

Applying Eq. (12), the transition amplitude for the projectile electron in the *time-dependent distorted-wave approximation* is

$$\mathscr{T}_{fi} \simeq \int dt\,\Big(\psi^{(-)}_{\alpha f}(t), V_\beta\,\psi^{(+)}_{\alpha i}(t)\Big)\,, \tag{14}$$

which is an expression widely used in laser-assisted scattering [49–51].

### C. Entrance-channel wave function

After obtaining the transition amplitude (14) for the scattering process, the next step is to obtain the entrance-channel wave function $\psi^{(+)}_{\alpha i}(t)$ satisfying the initial condition (13). Since the collision occurs in the presence of the laser pulse, we assume that the electron pulse adiabatically enters the interaction region in which the laser, electron, and atom beams overlap. Therefore, the state for the incident electron is represented by a Volkov wave (in the length gauge) [52]:

$$\begin{aligned} \chi_0(t) = (2\pi)^{-3/2}\; & e^{\,i\left[\boldsymbol{k}_0\cdot(\boldsymbol{x}_0-\boldsymbol{\alpha}(t))-E_0t-\int_{-\infty}^{t}dt'\frac{\boldsymbol{A}^2(t')}{2m_0c^2}\right]} \\ & \times e^{\,i\frac{1}{c}\boldsymbol{A}(t)\cdot\boldsymbol{x}_0}\,, \end{aligned} \tag{15}$$

where $\boldsymbol{x}_0$ is the spatial coordinate of the projectile electron, $m_0$ is the electron mass, $\boldsymbol{A}(t)$ is the vector potential of the laser pulse, $c$ is the speed of light, $E_0 = \boldsymbol{k}_0^2/2m_0$, and $\boldsymbol{\alpha}(t)$ is the classical displacement vector of the electron in the laser field:

$$\boldsymbol{\alpha}(t) = \frac{1}{m_0 c}\int_{-\infty}^{t} dt'\,\boldsymbol{A}(t')\,. \tag{16}$$

Note that $\boldsymbol{k}_0$ is the canonical momentum of the projectile electron in the laser field. However, since we have assumed that the electron adiabatically transforms from a field-free state to the Volkov wave and employed the dipole approximation, the canonical momentum is equal to the kinetic momentum of the incident electron before entering the interaction region [54].

The atomic state is comprised of its external center-of-mass motion, described by $\chi_1(t)$, and its internal (electronic) state, described by $\psi_1(t)$. We consider a neutral target, so its external motion is described by a plane wave:

$$\chi_1(t) = (2\pi)^{-3/2}\; e^{\,i(\boldsymbol{k}_1\cdot\boldsymbol{x}_1 - E_1 t)}\,, \tag{17}$$

where $\boldsymbol{x}_1$ is the coordinate of the center of mass of the target, and $E_1 = \boldsymbol{k}_1^2/2m_1$ is the kinetic energy of the target. The electronic wave function $\psi_1(t)$ is expanded in terms of the electronic eigenstates, $\phi_n$, of $H_1$:

$$\psi_1(t) = \sum_n C_n(t)\,\phi_n\,e^{-i\omega_n t}\,, \tag{18}$$

where $n$ denotes a collection of quantum numbers characterizing each eigenstate, and $C_n(t)$ and $\omega_n$ are the amplitude and eigenvalue of $\phi_n$, respectively. Note that $C_n(t)$ depends on time because of the presence of the pump laser, and its magnitude reflects the time-dependent population of $\phi_n$.

In order to properly describe the time-resolved scattering, the projectile electron and target have to be localized in space and time in order that the moment of collision can be well defined. This localization can be attained by describing the incident electron and the target wave functions as *wave-packet integrals* that superpose the entrance states [Eqs. (15) and (17)] of the incident electron and target [42, 43, 53, 56]. Hence, the wave packet corresponding to the initial condition is

$$\psi_{\alpha i}^{(+)}(t) = \int d\boldsymbol{k}_0\,d\boldsymbol{k}_1\,a_0(\boldsymbol{k}_0)\,a_1(\boldsymbol{k}_1)\,e^{-i\boldsymbol{k}_1\cdot\boldsymbol{b}}\,\chi_0\,\chi_1\,\psi_1\,, \tag{19}$$

where $a_0(\boldsymbol{k}_0)$ and $a_1(\boldsymbol{k}_1)$ are the respective momentum amplitudes of the projectile electron and target, and $\boldsymbol{b}$ is the position vector of the target. Rather than assuming a head-on collision, we treat the collision more generally by assuming the target is localized at position $\boldsymbol{b}$; later, an average over the positions of targets in an ensemble will be implemented. Note that the magnitude $|\boldsymbol{b}_\perp|$ of the transverse components of the position vector is the impact parameter of the collision; also, the longitudinal component $b_\parallel$ affects the time of collision.

### D. Exit-channel wave function

The exit-channel wave function $\psi_{\alpha f}^{(-)}$ depends on the way the scattering system interacts with $V_\alpha(t)$ after the collision takes place. We assume the duration of the laser pulse is much longer than that of the electron pulse; thus the collision process has finished before the completion of the population transfer. Therefore, the effect of the laser interaction on the exit-channel wave function should be taken into account. It is assumed that the scattered electron exits the reaction region adiabatically, so the final kinetic momentum $\boldsymbol{k}_a$ equals the canonical momentum after the collision. The state of the scattered electron is described by a Volkov wave,

$$\chi_a(t) = (2\pi)^{-3/2}\;e^{i\left[\boldsymbol{k}_a\cdot(\boldsymbol{x}_0-\boldsymbol{\alpha}(t))-E_a t+\int_t^\infty dt'\,\frac{\boldsymbol{A}^2(t')}{2m_0c^2}\right]} \times e^{i\frac{1}{c}\boldsymbol{A}(t)\cdot\boldsymbol{x}_0}\,, \tag{20}$$

and the final state of the target is described by a plane wave,

$$\chi_b(t) = (2\pi)^{-3/2}\;e^{i(\boldsymbol{k}_b\cdot\boldsymbol{x}_1-E_b t)}\,. \tag{21}$$

Here, $E_a = \boldsymbol{k}_a^2/2m_0$ and $E_b = \boldsymbol{k}_b^2/2m_1$ are the kinetic energies of the scattered electron and target, respectively.

For the target electronic state, besides the assumption that the duration of the electron pulse is shorter than that of the laser pulse, we further assume the laser pulse is long enough that its envelope and frequency change little during the collision, while the short laser period ($\approx 2.1$ fs) compared to its duration ($\approx 2$ ps) allows the laser pulse to be treated as a plane wave during the collision. Thus, the target electronic state $\psi_b(t)$ can be approximated by a Floquet state,

$$\psi_b(t) \simeq e^{-i\eta_f t}\sum_{mj} a_{mj}^f\,\phi_m\,e^{-ij\omega_{\rm ins}t}\,, \tag{22}$$

where $\eta_f$ is the quasi-energy, $a_{mj}^f$ are the expansion coefficients of the Floquet state $f$, and $\omega_{\rm ins}$ is the *instantaneous frequency* of the (chirped) laser pulse at the moment of collision. The summations include all field-free bound eigenstates $\phi_m$ and the Floquet-Fourier components $j$. Note that $a_{mj}^f$ and $\eta_f$ depend on the laser parameters (such as the instantaneous amplitude, frequency, and phase), so $\psi_b(t)$ is different at each pump-probe delay time.

Finally, the exit-channel wave function is approximated by the product of the exit states of the reaction products:

$$\psi_{\alpha f}^{(-)}(t) \simeq \chi_a\,\chi_b\,\psi_b\,. \tag{23}$$

### E. Transition amplitudes

After obtaining the entrance- and exit-channel wave functions, the transition amplitude $\mathscr{T}_{fi}$ can be evaluated by substituting Eqs. (19) and (23) into Eq. (14) to yield

$$\mathscr{T}_{fi} \simeq \int dt \int d\boldsymbol{k}_0\,d\boldsymbol{k}_1\,a_0(\boldsymbol{k}_0)\,a_1(\boldsymbol{k}_1)\,e^{-i\boldsymbol{k}_1\cdot\boldsymbol{b}} \times\left(\chi_a\,\chi_b\,\psi_b, V_\beta\,\chi_0\,\chi_1\,\psi_1\right)\,. \tag{24}$$

In the following, we further simplify and analyze Eq. (24). In order to perform the temporal integral, the Fourier transform of $C_n(t)$ [see Eq. (18)] is introduced:

$$C_n(t) = \frac{1}{\sqrt{2\pi}}\int_{-\infty}^{\infty} d\nu\,e^{-i\nu t}\,C_n(\nu)\,. \tag{25}$$

For time-resolved scattering, $\mathscr{T}_{fi}$ depends on the collision time. The relative delay between the pump laser and the probe electron can be modeled by displacing $\psi_1(t)$ in time, so the onset of the laser pulse at the origin precedes the electron pulse by a time $t_d$. The temporal displacement of the target at $\boldsymbol{b}$ is denoted by $t_1$. Moreover, due

to the quasi-monochromaticity of the laser pulse, the displacement vector for the projectile electron [see Eq. (16)] is approximated by the one for a plane wave:

$$\boldsymbol{\alpha}(t) \simeq \boldsymbol{\alpha}_{\rm ins}\, \cos\left(\omega_{\rm ins} t\right)\,, \tag{26}$$

where $\boldsymbol{\alpha}_{\rm ins}$ is the instantaneous amplitude of the displacement vector at the moment of collision. The carrier-envelope phase is irrelevant, as its effect is small for a many-cycle pulse. Thus it is excluded from Eq. (26). Substituting Eqs. (25) and (26) into Eq. (24), the time-dependent factors in the integrand for $\mathscr{T}_{fi}$ are:

$$\begin{aligned}&\int dt\, e^{i(\varepsilon_f-\varepsilon_i)t}\, e^{-i\boldsymbol{s}\cdot\boldsymbol{\alpha}(t)}\cdots \\ &\simeq \sum_{\mu=-\infty}^{\infty} (-i)^\mu J_\mu(\boldsymbol{s}\cdot\boldsymbol{\alpha}_{\rm ins})\,(2\pi)\,\delta(\varepsilon_f-\varepsilon_i-\mu\,\omega_{\rm ins})\cdots\,,\end{aligned} \tag{27}$$

where $\varepsilon_f \equiv E_a + E_b + \eta_f + j\omega_{\rm ins}$, $\varepsilon_i \equiv E_0 + E_1 + \omega_n + \nu$, $\boldsymbol{s} \equiv \boldsymbol{k}_0 - \boldsymbol{k}_a$ is the momentum transfer, $J_\mu$ is the $\mu$th order Bessel function, and the ellipses on either side of Eq. (27) denote the time-independent factors. Instead of a single $\delta$-function for the conservation of energy in the case of a time-independent Hamiltonian, the temporal integral yields a series of energy $\delta$-functions representing the absorption or emission of photons with frequency $\omega_{\rm ins}$ by the laser-driven scattering system during the collision.

Since in the dipole approximation the total canonical momentum is conserved during the collision, a corresponding $\delta$-function can be factored from $\mathscr{T}_{fi}$. Therefore, one obtains

$$\begin{aligned}\mathscr{T}_{fi} \simeq{}& (2\pi)^{1/2}\int d\boldsymbol{k}_0\, d\boldsymbol{k}_1\, a_0(\boldsymbol{k}_0)\, a_1(\boldsymbol{k}_1)\, e^{-i\boldsymbol{k}_1\cdot\boldsymbol{b}} \\ &\times \delta\left(\mathcal{P}_f-\mathcal{P}_i\right)\sum_{mj} a_{mj}^{f\,*}\sum_n \int d\nu\, C_n(\nu)\, e^{-i(\omega_n+\nu)t_1} \\ &\times T_{mn}\sum_\mu (-i)^\mu J_\mu(\boldsymbol{\alpha}_{\rm ins}\cdot\boldsymbol{s})\,\delta(\varepsilon_f-\varepsilon_i-\mu\,\omega_{\rm ins})\,,\end{aligned} \tag{28}$$

where $\mathcal{P}_i \equiv \boldsymbol{k}_0 + \boldsymbol{k}_1$ and $\mathcal{P}_f \equiv \boldsymbol{k}_a + \boldsymbol{k}_b$ are the respective initial and final linear momenta of the scattering system, and

$$T_{mn} \equiv \frac{1}{(2\pi)^3}\int d\boldsymbol{y}\, e^{i\boldsymbol{s}\cdot\boldsymbol{y}}\, \left(\phi_m, V_\beta\, \phi_n\right) \tag{29}$$

is the usual Born approximation transition amplitude from the eigenstate $n$ to $m$ in the center-of-mass frame. The inner product in Eq. (29) involves an integration over all target electron coordinates. As shown in Eq. (28), the time-resolved transition amplitude $\mathscr{T}_{fi}$ from the non-stationary state $\psi_1(t)$ to the final state $\psi_b(t)$ is a coherent superposition of $T_{mn}$ amplitudes weighted by the corresponding amplitudes of the projectile electron and target ($a_0$, $a_1$, and $C_n$). These multiple momentum and energy components superposed in the coherent wave packet produce interferences between various transitions $T_{mn}$, thereby resulting in a delay-dependent scattering amplitude (28).

### F. Scattering probability and ensemble average

The scattering probabilities for the projectile electrons are calculated from the transition amplitudes in Eq. (28),

$$\mathscr{P} = \sum_f \int d\boldsymbol{k}_b\, d\boldsymbol{k}_a\, |\mathscr{T}_{fi}|^2\,, \tag{30}$$

where the ranges of the integrations over the final momenta $\boldsymbol{k}_a$ and $\boldsymbol{k}_b$ and the number of final states $f$ in the summation are set by experimental observables. We assume energy- and angle-resolved measurements for the scattered electrons, so unresolved channels have to be summed in order to calculate the diffraction patterns. Hence, we define the *doubly differential probability*, namely, the probability density for an electron scattered into a differential solid angle per unit energy interval, as

$$\frac{d^2\mathscr{P}}{dE_a d\hat{\boldsymbol{k}}_a} \equiv \sum_f \int d\boldsymbol{k}_b\, m_0|\boldsymbol{k}_a|\,|\mathscr{T}_{fi}|^2\,. \tag{31}$$

It represents the diffraction pattern observed in an experiment having the necessary resolution.

Since the positions of the projectile electrons and targets are not controlled to atomic precision in gas-phase scattering, the differential probability needs to be averaged over the positions $\boldsymbol{b}$ of targets in an ensemble [57]:

$$\left\langle \frac{d^2\mathscr{P}}{dE_a d\hat{\boldsymbol{k}}_a}\right\rangle \equiv \int d\boldsymbol{b}\,\rho(\boldsymbol{b})\,\frac{d^2\mathscr{P}}{dE_a d\hat{\boldsymbol{k}}_a}\,, \tag{32}$$

where $\rho(\boldsymbol{b})$ is the density distribution of the target ensemble. We assume the targets are uniformly distributed in the transverse direction (with respect to the propagation axis of the incident electrons) and that the transverse size of the ensemble is much larger than the transverse dimension of the electron pulse. On the other hand, the targets are assumed to be well-confined along the longitudinal direction in order to reduce the effect of the mismatch in the group velocities of the laser and electron pulses. This confinement of the targets, in principle, can be achieved by a narrow focus of the laser pulses so that only targets within the focus undergo population transfer. Hence, assuming the pump-probe delay for each target is independent of its transverse position $\boldsymbol{b}_\perp$ in the ensemble, integration over $\boldsymbol{b}_\perp$ yields an additional $\delta$ function in the ensemble-averaged differential probability,

$$\begin{aligned}&\int d\boldsymbol{b}\,\rho(\boldsymbol{b})\, e^{i(\boldsymbol{k}_1'-\boldsymbol{k}_1)\cdot\boldsymbol{b}}\cdots \\ &= (2\pi)^2\rho_\perp\,\delta(\boldsymbol{k}_{1\perp}'-\boldsymbol{k}_{1\perp})\int db_\parallel\,\rho_\parallel(b_\parallel)\, e^{i(k_{1\parallel}'-k_{1\parallel})b_\parallel}\cdots\,,\end{aligned} \tag{33}$$

where $\boldsymbol{k}_1$ and $\boldsymbol{k}_1'$ are two momentum components in the target wave packet, $\rho_\perp$ is the transverse area density of the targets, the subscripts $\perp$ and $\parallel$ respectively denote the transverse and longitudinal components, and the ellipses denote the $\boldsymbol{b}_\perp$-independent factors in $\mathscr{P}$. Here

we have assumed that the target density can be factorized into perpendicular and parallel parts, namely, $\rho(\boldsymbol{b}) = \rho_\perp \times \rho_\parallel(b_\parallel)$. The $\delta$-function in Eq. (33) implies that the transverse position of the target relative to the incident electron for each individual collision has no effect on the ensemble-averaged scattering probability.

In order to integrate over $b_\parallel$, further assumptions about the dependence of $\mathscr{P}$ on $b_\parallel$ must be made. Given a delay $t_d$ between the laser and electron pulses at the origin, the collision time for a target depends on its parallel position $b_\parallel$ because of the velocity mismatch. Supposing that the group velocity of the laser pulse is the speed of light, the onset of the population transfer of the target at $b_\parallel$ is delayed by $b_\parallel/c$ compared with the target at the origin ($\boldsymbol{b} = 0$), so the time displacement $t_1$ of $\psi_1(t)$ may be approximated as

$$t_1(b_\parallel) \simeq t_d - \frac{b_\parallel}{c}\,. \tag{34}$$

Furthermore, we assume the longitudinal distribution $\rho_\parallel$ is a Gaussian distribution with a width $\sigma_b$ (*i.e.*, $\rho_\parallel(b_\parallel) = e^{-b_\parallel^2/2\sigma_b^2}/\sqrt{2\pi}\sigma_b$). Thus, the integral on the right-hand side of Eq. (33) yields

$$\begin{aligned}&\int db_\parallel\, \rho_\parallel(b_\parallel)\, e^{i(k'_{1\parallel}-k_{1\parallel})b_\parallel}\, e^{-i(\omega_n+\nu)t_1}\, e^{i(\omega_{n'}+\nu')t_1}\cdots\\ &\simeq e^{i(\omega_{n'}-\omega_n+\nu'-\nu)t_d}\, e^{-\frac{1}{2}\sigma_b^2\left(k'_{1\parallel}-k_{1\parallel}-\frac{\omega_{n'n}+\Delta\nu}{c}\right)^2}\cdots\,,\end{aligned} \tag{35}$$

where $\{\omega_n, \nu\}$ and $\{\omega_{n'}, \nu'\}$ are two sets of frequency components of the target electronic state [see Eqs. (18) and (25)], $\omega_{n'n} \equiv \omega_{n'} - \omega_n$, $\Delta\nu \equiv \nu' - \nu$, and the ellipses denote the factors in $\mathscr{P}$ that are independent of $b_\parallel$. Since, as aforementioned, the time dependence of the scattering probability results from the interference of scattering amplitudes [see the first exponential factor on the right-hand side of Eq. (35)], the longitudinal size $\sigma_b$ of the ensemble effectively constrains the interference among the momentum and energy components [see the second exponential factor on the right-hand side of Eq. (35)], and, therefore, the temporal resolution.

Finally, the ensemble-averaged differential probability can be simplified using the energy and momentum $\delta$-functions. Since similar procedures have been detailed in Refs. [42, 43], we only summarize the result below:

$$\begin{aligned}\left\langle \frac{d^2\mathscr{P}}{dE_a d\hat{\boldsymbol{k}}_a}\right\rangle &\simeq \rho_\perp\,(2\pi)^3\, m_0|\boldsymbol{k}_a| \sum_{m'j'} a^f_{m'j'} \sum_{n'}\\ &\times \int d\nu'\, C^*_{n'}(\nu')\, e^{i(\omega_{n'}+\nu')t_d} \sum_{mj} a^{f\,*}_{mj} \sum_{n}\\ &\times \int d\nu\, C_n(\nu)\, e^{-i(\omega_n+\nu)t_d} \sum_{\mu'\mu} \int d\boldsymbol{k}_{0\perp}\, d\boldsymbol{k}_1\\ &\times a_0(|\boldsymbol{k}_a| + \Delta k, \boldsymbol{k}_{0\perp})\, a_0^*(|\boldsymbol{k}_a| + \Delta k + \Delta\kappa, \boldsymbol{k}_{0\perp})\\ &\times a_1(\boldsymbol{k}_1)\, a_1^*(k_{1\parallel} - \Delta\kappa, \boldsymbol{k}_{1\perp})\, e^{-\frac{1}{2}\sigma_b^2\left(\Delta\kappa - \frac{\omega_{n'n}+\Delta\nu}{c}\right)^2}\\ &\times \frac{1}{|k_{0\parallel}/m_0 - (k_{0\parallel} + k_{1\parallel} - k_{a\parallel})/m_1|}\\ &\times \frac{1}{|(k_{0\parallel} + \Delta\kappa)/m_0 - (k_{1\parallel} - \Delta\kappa)/m_1|}\\ &\times i^{\mu'} J_{\mu'}(\boldsymbol{\alpha}_{\rm ins}\cdot\boldsymbol{s}')\,(-i)^{\mu} J_{\mu}(\boldsymbol{\alpha}_{\rm ins}\cdot\boldsymbol{s})\, T^*_{m'n'}\, T_{mn}\,.\end{aligned} \tag{36}$$

One sees that the amplitudes $a_0$, $a_1$, $C_n$, and $T_{mn}$ appear in pairs upon calculating the absolute square of $\mathscr{T}_{fi}$. Moreover, the amplitudes $a_0$ and $a_1$ are shifted by $\Delta\kappa$ with respect to their counterparts $a_0^*$ and $a_1^*$, because, as energy is exchanged between the projectile electron and target (*e.g.*, $\omega_{n'n} \neq 0$), the conservation laws couple the components in the wave packet that interfere. The overall shift $\Delta k$ of $a_0$ with respect to $|\boldsymbol{k}_a|$ is due to the conservation of energy between the reactants and the products. Note that these shifts depend on the initial and final states ($n$, $n'$, $m$ and $m'$) as well as the number of photons exchanged (*i.e.*, $j$, $j'$, $\mu$ and $\mu'$) during the collision. The fractions are the flux factors, taking into account the collision rate for each combination of momentum components. For a high-energy electron wave packet having a narrow momentum spread, they are insensitive to the momentum distributions in the wave packets.

## III. APPLICATION AND NUMERICAL PROCEDURES FOR LITHIUM ATOMS

In this section we apply the general theory to the special case in which the valence electrons of the lithium atoms are transferred from the $2s$ to the $2p$ state by means of a frequency-swept laser pulse. Details of our simulations are also discussed.

### A. Eigenstates of the lithium atom

The eigenstates of the lithium atom are obtained by solving the Schrödinger equation with the Herman-Skillman potential [58]. This potential is obtained by solving the Hartree-Fock equation for the lithium atom under the following approximations. First, the central field approximation is used for the electrons, so the orbital wave function $o_{plm_l}$ for the $j$-th electron, $1 \leq j \leq 3$,

is factorized into radial and angular parts:

$$o_{plm_l}(\boldsymbol{r}_j) = R_{pl}(|\boldsymbol{r}_j|)\, Y_{lm_l}(\hat{\boldsymbol{r}}_j)\,, \tag{37}$$

where $p$, $l$, and $m_l$ respectively are the principal, orbital angular momentum, and magnetic quantum numbers, $\boldsymbol{r}_j$ is the spatial coordinate of the $j$-th electron, and $Y_{lm_l}$ is a spherical harmonic. Second, the electron-electron potential is approximated by the Hartree-Fock-Slater (HFS) potential in which the exchange part of the potential is replaced by the one for a free-electron gas; also, the HFS potential is joined to the correct Coulombic asymptotic potential at large radii. Third, relativistic effects are neglected. The eigenstate $\phi_n$ of the lithium atom is then approximated by a Slater determinant that is antisymmetric under particle exchange.

Although the above approximations greatly simplify our calculations, the Herman-Skillman potential is unable to provide atomic structures with spectroscopic accuracy. Nonetheless, this potential serves our purposes well for the following reasons. First, gas-phase ultrafast electron diffraction has not as yet reached spectroscopic resolutions. Second, at present we are concerned with determining whether qualitative features of target electronic motions are reflected in the time- and energy-resolved diffraction patterns; these qualitative general features are unlikely to be significantly altered in simulations having higher accuracy. Third, the HFS potential is known to provide satisfactory results for such light atoms as lithium in which many-electron and spin-orbit effects are small.

### B. Population transfer in the lithium atom

After obtaining the lithium eigenstates, we proceed to simulate the process of laser-driven population transfer by solving the time-dependent Schrödinger equation. The electric field of the laser pulse is assumed to have a Gaussian profile:

$$\boldsymbol{E}(t) = \boldsymbol{F}_0\, e^{-\frac{(t-t_c)^2}{2\sigma^2}} \cos\left(\omega_0(t-t_c) + \frac{1}{2}\beta(t-t_c)^2\right), \tag{38}$$

where $\boldsymbol{F}_0$ is the peak amplitude, $t_c$ is the peak position in time, $\sigma$ is the Gaussian width, $\omega_0$ is the carrier frequency, and $\beta$ denotes the chirp of the laser pulse. The instantaneous frequency, $\omega_{\rm ins}$, at a time $t$ is given by the time derivative of the phase of the field at that time,

$$\omega_{\rm ins} = \omega_0 + \beta(t-t_c)\,. \tag{39}$$

The pump laser pulse is assumed to be linearly polarized along the $z$ axis (see Fig. 1). In our simulations, $F_0 = 2.35\times10^{-5}$ a.u., the full width at half maximum (FWHM) duration is 2.0 ps ($\sigma = 0.85$ ps), $\beta = 1.5\times10^{-3}$ eV/ps, and the carrier frequency is set to be the $2s$-$2p$ resonant frequency ($\omega_0 = 1.946$ eV).

We consider the single active electron approximation for the valence electron, since for a weak pulse the population transfer is largely a single electron process. The wave function $\psi_1(t)$ is expanded in the eigenstates of the lithium atom [see Eq. (18)], so the Schrödinger equation is reduced to a system of linear differential equations for the expansion coefficients $C_n(t)$. These coefficients are then propagated in time using the fourth-order Runge-Kutta method. The initial state is the ground state of the lithium atom. The time scale of the population transfer in our simulations takes a few picoseconds, which is shorter than the lifetime of the $2p$ state ($\approx 27.1$ ns [59]), so spontaneous emission from the $2p$ state is not modeled in the simulations. Furthermore, since three photons are required to ionize the lithium atoms, for our weak laser pulses multiphoton ionization can be neglected.

### C. Incident electron pulses

We consider the momentum amplitude $a_0(\boldsymbol{k}_0)$ of the incident electron to have a Gaussian distribution. The longitudinal and transverse widths of the profile $|a_0(\boldsymbol{k}_0)|^2$ are set by the pulse duration and angular divergence, respectively. Moreover, we assume $a_0(\boldsymbol{k}_0)$ is transform limited (*i.e.*, chirpless). In our simulations, the incident electrons move in the positive $x$ direction with a central kinetic energy 10.000 keV in the laboratory frame, and their angular divergence is $\pm10^{-4}$ rad. The corresponding central momentum is $|\boldsymbol{p}_0| = 27.111$ a.u. In our simulations, two pulse durations are used: 1 fs and 100 fs (FWHM).

Regarding our assumption that the incident electron pulse is chirpless, we note that transform-limited pulses are uncommon in practice, for several reasons. Specifically, the vacuum is dispersive for electrons. Also, an additional chirp may be introduced by space charge effects or by the mechanism for generating ultrashort electron pulses (*e.g.*, see Ref. [60]). This is why most techniques for producing ultrashort electron pulses include methods for compensating such effects such that in the interaction region at the instant of collision the pulses are as close to chirpless as possible, *i.e.*, as short as possible (see Refs. [8, 33, 34]). For this reason, we employ transform-limited pulses in our simulations. Moreover, we have found that, as long as the pulse duration is shorter than the time scale of the target electronic motion, a mild linear chirp only reduces the contrast (or visibility) of the temporal oscillation observed in the diffraction patterns.

### D. Scattering probabilities

Although the ensemble-averaged differential probabilities can be calculated using Eq. (36), the parameters of our simulations allow for further simplifications of that equation. First, the absorption and emission of photons by the projectile electron are neglected. We have seen

in Eq. (28) that the amplitude for absorption or emission of $\mu$ photons is proportional to $J_\mu(\boldsymbol{\alpha}_{\rm ins}\cdot\boldsymbol{s})$. For a weak field ($F_0 \approx 10^{-5}$ a.u.), the amplitude of the displacement vector $\boldsymbol{\alpha}_{\rm ins}$ is small ($\lesssim 0.005$ a.u. in our case). In addition, owing to the high energy of the incident electrons ($E_0 = 10.000$ keV), they are primarily scattered in the forward direction, so that the magnitudes of the momentum transfers are small. Consequently, the argument of the Bessel function is much less than unity, so $J_\mu(\boldsymbol{\alpha}_{\rm ins}\cdot\boldsymbol{s}) \approx 0$ if $\mu \neq 0$. Hence, the probabilities for photon emission or absorption can be neglected for the projectile electrons and thus we have also approximated $J_0(\boldsymbol{\alpha}_{\rm ins}\cdot\boldsymbol{s}) \approx 1$ in the simulations.

Second, we assume the lithium atoms are well localized in space, so their momentum amplitudes $a_1(\boldsymbol{k}_1)$ have a broad width such that $a_1(\boldsymbol{k}_1)$ is insensitive to the variation of $\Delta\kappa$ in the wave-packet integral:

$$a_1(k_{1\parallel} - \Delta\kappa, \boldsymbol{k}_{1\perp}) \simeq a_1(k_{1\parallel}, \boldsymbol{k}_{1\perp})\,. \tag{40}$$

Furthermore, we assume that the quantities depending on the target momentum $\boldsymbol{k}_1$ in Eq. (36) (*e.g.*, $T_{mn}$) are insensitive to the variation of $\boldsymbol{k}_1$ within the width of the momentum distribution. Therefore, these quantities can be evaluated approximately at the central momentum $\boldsymbol{p}_1$ of the targets. Under the above assumptions the $\boldsymbol{k}_1$ integral can be performed analytically, rendering an expression independent of the details of the target wave packet except for its localization in space.

Third, although the target states $\psi_b(t)$ of the exit channel should be the Floquet states [see Eq. (22)], the calculation can be simplified by considering the effects of the dressing of the lithium atom states by the pump laser. We found that, owing to the weak laser intensity and the small detuning, the dressing is effectively limited to the $2s$ and $2p$ states. Therefore, the $2s$ and $2p$ states can be considered as an isolated two-state system, and the final state $\psi_b(t)$ can be approximated by considering only the dressing of the two-state system and assuming no dressing for the other excited states of the lithium atom.

Fourth, we found that during the entire population transfer process the populations in excited states other than $2p$ are negligible. Hence, in calculating the scattering probabilities, $\psi_1(t)$ includes only the $\phi_{2s}$ and $\phi_{2p}$ states. We further assume that the target density is $10^{10}$ cm$^{-3}$ [61] and that the longitudinal size of the ensemble has a small thickness of 50 $\mu$m; hence the velocity mismatch effects are minimal. Moreover, techniques have been used to further reduce velocity mismatch effects [20, 62], so we set $\sigma_b \approx 0$. We consider the lithium atoms to have the thermal energy of room temperature, which is much smaller than the energy of the incident electron, so we set $\boldsymbol{p}_1 = 0$.

Finally, since the mass of the projectile electron is much smaller than that of the target ($m_0 \ll m_1$), the projectile-target interaction is approximated by

$$V_\beta \simeq -\frac{3}{|\boldsymbol{y}|} + \sum_{j=1}^{3}\frac{1}{|\boldsymbol{y}-\boldsymbol{r}_j|}\,, \tag{41}$$

where $\boldsymbol{y} \equiv \boldsymbol{x}_0 - \boldsymbol{x}_1$ is the relative distance between the projectile electron and the target. Then the expression for $T_{mn}$ can be calculated by substituting Eq. (41) into Eq. (29):

$$T_{mn} \simeq \frac{1}{(2\pi)^2}\frac{2}{\boldsymbol{s}^2}\Big[-3\,\delta_{mn} + \sum_{j=1}^{3}\int d\{\boldsymbol{r}_j\}\, e^{i\boldsymbol{s}\cdot\boldsymbol{r}_j}\,\phi_m^*\,\phi_n\Big]\,. \tag{42}$$

Since the orbital wave function is factorized into its radial and angular parts [see Eq. (37)], the integration over electron coordinates $\{\boldsymbol{r}_j\}$ can accordingly be calculated separately. The angular expression can be found in [42] and the radial part is done numerically. Moreover, the exchange effect is unimportant, as the exchange integral is negligible [6].

## IV. RESULTS AND DISCUSSION

### A. Population Transfer in Lithium Atoms

The results of the population transfers in the lithium atoms are shown in Fig. 2. The $2s$ and $2p$ populations as a function of time are presented in Fig. 2(a), and the corresponding amplitudes $C_n$ in the time and frequency domains are shown in Figs. 2(b) and (c), respectively. The spectra in Fig. 2(c) are presented in atomic units of energy. For the laser parameters used here (see Sec. III B), the $2s$ and $2p$ populations change monotonically, and the process lasts about 3 ps. Essentially 100% of the population is moved from the $2s$ to the $2p$ state, and no appreciable population is observed in other excited states during the pump process. The oscillations of $C_n(\nu)$ are mainly due to the shift of the center of the laser pulse in the time domain to $t_c = 3.6$ ps, which yields a phase $e^{i\nu t_c}$ that oscillates in frequency with a period of $2\pi/t_c = 0.42\times10^{-4}$ a.u. The widths of $C_n(\nu)$ are set by the time scale of the population transfer. The envelopes of spectra are slightly shifted toward negative frequency, which results from the dynamic Stark effect (*i.e.*, the dressing of the lithium eigenstates).

### B. Time-, Angle-, and Energy-Resolved Ultrafast Electron Diffraction of 100-fs Electron Pulses

We first present the time- and angle-resolved spectra for 100-fs electron pulses, whose duration is short enough to map the population transfer in lithium atoms. Figure 3 shows the ensemble-averaged doubly differential probability (EADDP) at four time delays: $t_d = 1.0$, 3.0, 4.0, and 6.0 ps. The abscissa and ordinate respectively represent the energies $E_a$ and angles $\theta$ of the scattered electrons, and the azimuthal scattering angle is set to be $\varphi = 0°$ (see Fig. 1). Owing to the narrow bandwidth of the probe pulse ($\approx 0.018$ eV), which enables state-resolved measurements, the spectra exhibit

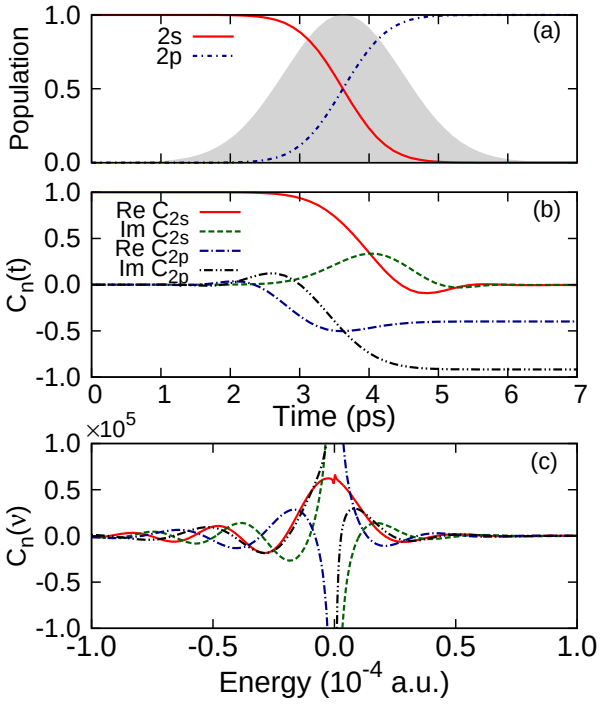


FIG. 2. (Color online) (a) Populations of the $2s$ and $2p$ states of lithium atoms undergoing laser-driven population transfer as a function of time. The shaded area indicates the envelope of the electric field $\boldsymbol{E}(t)$ that drives the population transfer as a function of time. The laser pulse is centered at $t_c = 3.6$ ps with a Gaussian shape. (b-c) Amplitudes $C_n$ of the $2s$ and $2p$ states in the (b) time and (c) frequency domains. See Eqs. (18) and (25) for the definitions of $C_n(t)$ and $C_n(\nu)$, respectively. The real and imaginary parts of the $2s$ and $2p$ amplitudes are presented separately, as denoted by the legends in panel (b).

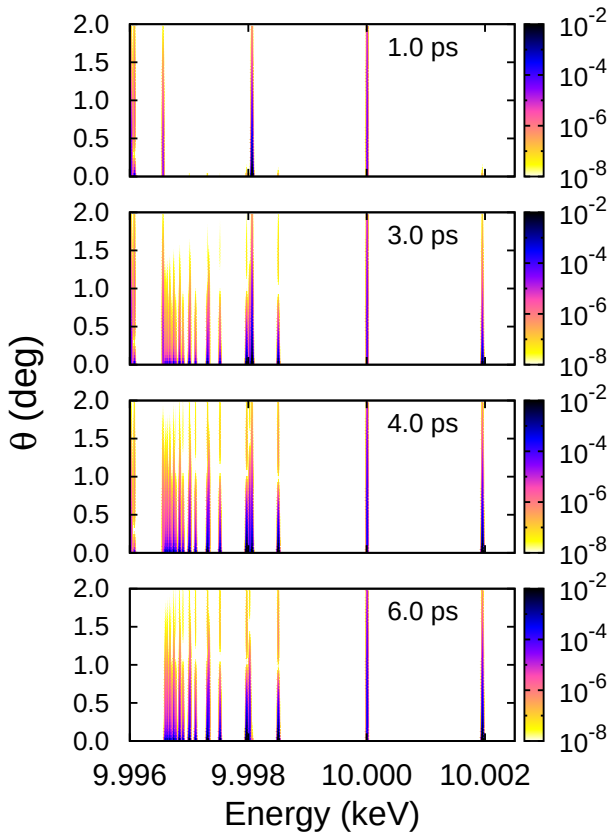


FIG. 3. (Color online) Ensemble-averaged doubly differential probabilities (EADDPs), $\langle d^2\mathscr{P}/dE_a d\hat{\boldsymbol{k}}_a\rangle$, for 100-fs electron pulses (FWHM) scattered from laser-driven lithium atoms at four time delays: $t_d = 1.0$, 3.0, 4.0, and 6.0 ps. The electronic population is driven from the $2s$ to $2p$ states by a chirped laser pulse (see Fig. 1). Each of the kinetic energies of the scattered electrons along the abscissa are plotted versus the scattering angle $\theta$ along the ordinate. The azimuthal scattering angle is $\varphi = 0°$. The energies of the incident electrons are centered at 10.000 keV.

peaks corresponding to transitions from the target state $\psi_1(t)$ to lithium eigenstates. The height of a peak in the $\theta$ direction indicates the extent of the angular distribution (or the magnitude of the momentum transfer) of the scattered electrons for that particular transition, whose scattering intensities at each value of $\theta$ are color coded on a logarithmic scale. As the energies of the incident electrons are centered at 10.000 keV, the excitation ($E_a < 10$ keV) and de-excitation ($E_a > 10$ keV) transitions are divided by the 10-keV peak. The 10-keV peak has the broadest angular extent owing to elastic scattering from the core electrons and the nucleus.

One observes that the angle-resolved spectrum as a function of time delay, $t_d$, reflects the change of the energy content and population in the lithium atoms. The number of peaks increases as the delay increases, while some peaks appearing at $t_d = 1.0$ ps wane. In particular, the emergence of the de-excitation peak close to 10.002 keV with increasing delay indicates the increase of electron excitation as a result of the pump process. Because of the predominant $2s$ and $2p$ populations at $t_d = 1.0$ and 6.0 ps, respectively, the corresponding spectra essentially represent scattering exclusively from the $2s$ and $2p$ states respectively [see Fig. 2(a)]. At $t_d = 1.0$ ps there are fewer peaks because higher energy is needed to excite the more deeply bound $2s$ state than the $2p$ state. At $t_d = 6.0$ ps, one can see a series of Rydberg transitions converging to the $2p$ ionization threshold at 3.548 eV; also, their angular extensions decrease as the transition approaches the threshold (see the discussion of Fig. 4 below). Excitation peaks above the $2p$ ionization threshold are embedded in the continuous $2p$-ionization channels. However, our simulations exclude these impact ionization channels since they can in principle be distinguished by means of two-electron coincidence measurements. Although the number of peaks varies with delay, the $\theta$ angular distribution of each transition is invariant. The nodes seen in some inelastic transitions remain at the same position, whereas the variations of the intensities of

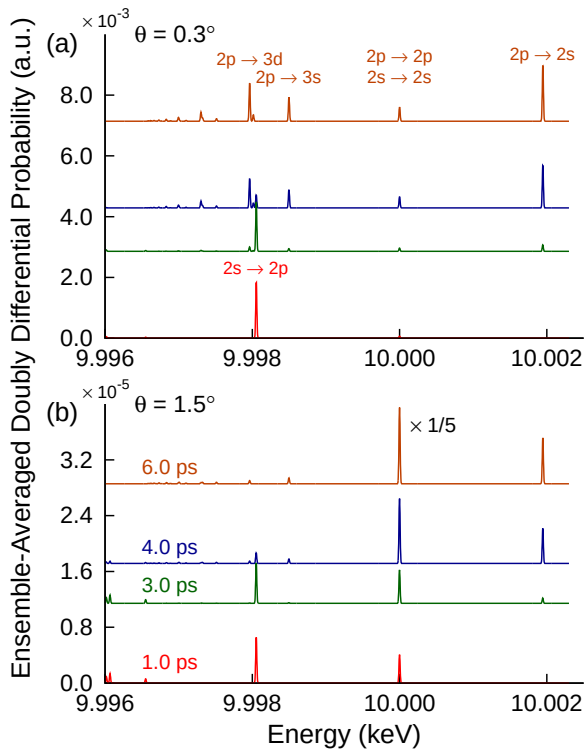


FIG. 4. (Color online) Lineout profiles of the EADDPs from Fig. 3 at (a) $\theta = 0.3°$ and (b) $\theta = 1.5°$ at four time delays: $t_d = 1.0$, 3.0, 4.0, and 6.0 ps. In order to avoid overlapping the peaks, the 3.0-, 4.0-, and 6.0-ps profiles are shifted upward respectively by $2.86\times10^{-3}$, $4.29\times10^{-3}$, and $7.14\times10^{-3}$ a.u. for $\theta = 0.3°$ and by $1.14\times10^{-5}$, $1.71\times10^{-5}$, and $2.86\times10^{-5}$ a.u. for $\theta = 1.5°$. The magnitude of the 10-keV peak at $\theta = 1.5°$ is reduced by a factor of 5 in panel (b). Transitions are assigned to dominant peaks of the spectrum in panel (a).

the peaks continuously follow the change of the population. The ensemble behaves like a mixed state comprising two different species, and the temporal behavior of the spectrum reveals the conversion of the populations in the two species by the chirped laser pulse.

For quantitative comparisons of the spectra, lineout profiles of Fig. 3 at small ($\theta = 0.3°$) and large ($\theta = 1.5°$) scattering angles are presented in Fig. 4 on a linear scale. The profiles corresponding to different delays are labeled in Fig. 4(b). The assignment of transitions for the dominant peaks are shown in Fig. 4(a). Owing to the strength of the elastic scattering transition, the 10-keV peaks at $\theta = 1.5°$ are reduced by a factor of 5, as indicated in Fig. 4(b). As can be seen in Fig. 4, the dominant inelastic transitions are dipole-allowed, such as $s-p$ and $p-d$ transitions. However, comparison of the spectra at the same delay with different $\theta$ in Figs. 4(a) and (b) shows that the relative contributions of the inelastic channels varies with the scattering angle $\theta$. More inelastic transitions can be seen in the spectra at the small angle, $\theta = 0.3°$, while only the $2s \to 2p$ and $2p \to 2s$ transitions are significant at the large scattering angle, $\theta = 1.5°$. In addition, the $2p \to 3s$ transition is weaker than the $2p \to 3d$ one at $\theta = 0.3°$, yet at $\theta = 1.5°$ their relative strength is reversed (although the overall magnitudes of both peaks decreases). This can be understood by analyzing the transition amplitude $T_{mn}$ [see Eq. (42)]. For small momentum transfer $\boldsymbol{s}$, the exponential function in Eq. (42) can be expanded as a power series in the momentum transfer:

$$e^{i\boldsymbol{s}\cdot\boldsymbol{r}_j} = 1 + i\boldsymbol{s}\cdot\boldsymbol{r}_j - \frac{1}{2!}(\boldsymbol{s}\cdot\boldsymbol{r}_j)^2 + \cdots . \qquad (43)$$

After integrating over electronic coordinates $\{\boldsymbol{r}_j\}$, each term in this expansion is associated with a different multipole order transition in the scattering amplitude. The first term, together with the scattering amplitude from the nucleus [the first term in the square bracket of Eq. (42)], is the monopole contribution to the scattering amplitude. The monopole term exists only if $\phi_m = \phi_n$. However, for a neutral target the two monopole amplitudes from the nucleus and the electrons cancel each other, so the 10-keV peak is smaller than the inelastic peaks at $\theta = 0.3°$. The next leading transition is the dipole term, which exists only if the final state $\phi_m$ has the opposite parity to that of the initial state $\phi_n$. Therefore, the dominant transitions in the forward direction are the dipole-allowed transitions [6].

To further understand the $\theta$ dependence of the relative strength for each channel, we note that in the Born approximation the scattering can be considered as a momentum-transfer process in which the initial state $\phi_n$ receives a momentum transfer $\boldsymbol{s}$ from the projectile electron. Its wave function in *momentum* space is thus displaced by the amount $\boldsymbol{s}$. The transition amplitude $T_{mn}$ is then proportional to the overlap between the wave functions of the displaced initial state $\phi_n$ and the final states $\phi_m$ [43]. Owing to the heaviness of the nucleus, the momentum transfer to the nucleus can be neglected in the internal coordinate frame. From this viewpoint, the angular distribution of the scattering probabilities indicates the relative momentum distributions of the initial and final states and how the momentum is transferred between the states. Since the deeper bound states $2s$ and $2p$ have broader momentum distributions and fewer nodes than most other excited states, as momentum is transferred from or to the $2s$ electron, the overlap between the two wave functions can still be substantial for large momentum transfers. The strongest inelastic peak is the $2s$-$2p$ transition. Likewise, the reversal of the relative scattering intensities of the $2p \to 3d$ and $2p \to 3s$ channels at $\theta = 0.3°$ and 1.5° can be attributed to the differences in their nodal structures and to the momentum distributions of the $3s$ and $3d$ final states. The $3d$ orbital has no nodes while the $3s$ orbital has two. Thus, less cancellation occurs in the transition amplitude for the $3d$ channel at small $\theta$. The wider momentum distribution of the $3s$ orbital than that of the $3d$ orbital allows more overlap of the $2p$ and $3s$ momentum wave functions at larger $\theta$.

Comparison of the spectra at different time delays with the same $\theta$ shows three types of temporal behaviors.

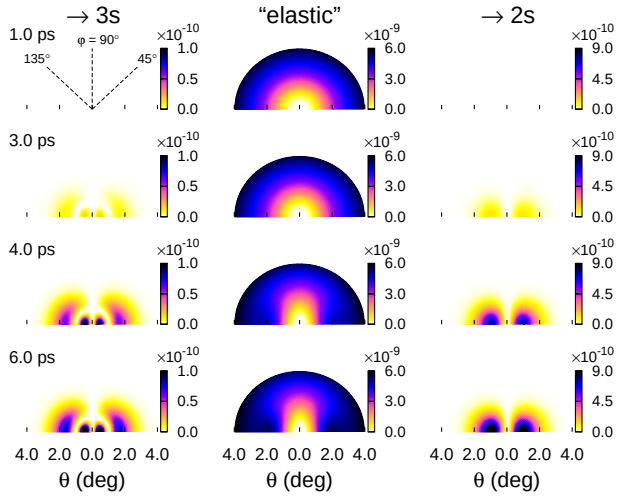


FIG. 5. (Color online) Modified diffraction images of the $2s$, $3s$, and "elastic" channels for 100-fs electron pulses scattered from laser-driven lithium atoms at four time delays: $t_d = 1.0$, 3.0, 4.0, and 6.0 ps. See Eq. (44) for the definition of the modified diffraction image, and Fig. 1 for the definitions of the scattering angles $\theta$ and $\varphi$. The $2s$ and $3s$ channels include all transitions labeled by those final states, as shown in Fig. 4. The elastic diffraction images correspond to the 10-keV peak in Fig. 4. Owing to symmetry, only the diffraction patterns in the upper half plane are shown.

The elastic scattering monotonically increases with delay, which shows that the $2p$ state has larger scattering probability than that of $2s$ state at both angles. Moreover, depending on the initial states, the inelastic peaks behave differently. Those peaks corresponding to a $2p$ initial state (*e.g.*, $2p \to 2s$) grow with the delay, and those corresponding to a $2s$ initial state (*e.g.*, $2s \to 2p$) decrease. This thus reflects the changes in the $2s$ and $2p$ populations.

### C. Energy-Resolved Ultrafast Electron Diffraction Images for 100-fs Electron Pulses

Provided one has adequate energy resolution and nonoverlapping transitions, one can isolate a few or even a particular transition from various scattering channels through energy-resolved measurements, thereby obtaining state-resolved diffraction images. One thus avoids possible loss of information on the target electronic motion resulting from averaging over transitions to final states having different energies. We present in Fig. 5 the diffraction images as a function of pump-probe time delay for three transitions that are well separated from others: the $2s$, elastic, and $3s$ channels. The *modified diffraction image* is defined by

$$\frac{d\mathscr{M}}{d\hat{\boldsymbol{k}}_a} \equiv \boldsymbol{s}^4 \int dE_a \left\langle \frac{d^2\mathscr{P}}{dE_a d\hat{\boldsymbol{k}}_a} \right\rangle . \tag{44}$$

Since the transition amplitude is strongly enhanced in the forward direction owing to the factor $1/\boldsymbol{s}^2$ [see Eq. (42)], we multiply the diffraction image by a factor $\boldsymbol{s}^4 \equiv (\boldsymbol{k}_a - \boldsymbol{p}_0)^4$ in Eq. (44) to suppress this effect. Thus the resulting distributions of the diffraction images at large $\theta$ can be better seen. (Recall that in elastic scattering $1/\boldsymbol{s}^4$ is the angular distribution of the Rutherford differential cross section.) The energy ranges used in Eq. (44) to calculate the modified diffraction images of the $2s$, elastic, and $3s$ channels are 10.0019-10.0020 keV, 9.99995-10.00005 keV, and 9.99843-9.99857 keV, respectively. Note that our results for the "elastic" channel include transitions to the various $m_l$ levels of the degenerate $2p$ state. As shown in Fig. 5, the diffraction images are sensitive functions of the pump-probe delay time, clearly demonstrating that ultrafast electrons provide the spatial and temporal resolution to map electronic motions in atoms. Moreover, the distinct diffraction patterns and temporal behaviors in the different channels imply the importance of differentiating the transitions in order to interpret the electronic motions.

Having discussed the interpretation of the $\theta$ angular distribution in Sec. IV B, here we focus on the $\varphi$ angular distributions for the state-resolved diffraction images. The $\varphi$ angular distributions of the elastic and inelastic channels behave differently, as shown in Fig. 5. The $2s$ and $3s$ channels have the same temporal behavior: their scattering intensities increase as the $2p$ population grows, and their $\varphi$ angular distributions remain unchanged. On the other hand, for the elastic channel both the scattering intensities and the $\varphi$ angular distribution vary with the delay. At $t_d = 1.0$ ps, the diffraction image shows an isotropic pattern for the elastic channel, indicating the spherical symmetry of the $2s$ state. Lack of monopole and dipole terms suppresses the modified scattering intensities in the forward direction. With increasing time delay, the angular distribution develops a two-fold symmetry. This change in the $\varphi$ angular distribution reflects the overlap of channels and the change of the orbital angular momentum imparted by the pump laser. Simply put, the scattered electrons carry the symmetry information about the target states.

In addition to the same $\varphi$ angular distributions, both $2s$ and $3s$ channels show a linear nodal structure along the $\varphi = 90°$ axis, which can be understood in terms of the symmetry of the scattering system and the parities of the electronic states. Since the Hamiltonian of the scattering system possesses mirror symmetry, the scattering amplitudes of two scattering geometries are associated with each other if the two geometries are related by mirror symmetry. In particular, consider the mirror operation with respect to the $x$-$y$ plane (*i.e.*, $z \to -z$) and the scattering geometry in which an incident electron moving in the positive $x$ direction with momentum $\boldsymbol{k}_0$ is scattered toward some direction with momentum $\boldsymbol{k}_a$. The scattering geometry obtained by the mirror operation is the one in which the electron is scattered toward the direction $\boldsymbol{k}'_a$, which is the mirror image of $\boldsymbol{k}_a$. Then one can show

that the $S$ matrix elements for these two geometries are related by,

$$\begin{aligned}&\langle \boldsymbol{k}_a, l_f\, m_f|\, S\,|\boldsymbol{k}_0, l_i\, m_i\rangle \\ =&(-1)^{l_i+l_f+m_i+m_f}\,\langle \boldsymbol{k}'_a, l_f\, m_f|\, S\,|\boldsymbol{k}_0, l_i\, m_i\rangle,\end{aligned} \tag{45}$$

as the target angular momentum state changes from $|l_i\, m_i\rangle$ to $|l_f\, m_f\rangle$. If the symmetry of the target state is changed such that $l_i + l_f + m_i + m_f$ is an odd number, then the scattering amplitude is also an odd function of $\boldsymbol{k}_a$ with respect to the $x$-$y$ plane. Consequently, the scattering amplitude must be zero in the symmetry plane, which is the reason the nodal line along $\varphi = 90°$ axis appears in the $2s$ and $3s$ channels. One can also see this from the viewpoint of momentum transfer. Since the parities of the initial $p$ and final $s$ states are opposite, the overlap between the displaced initial and the final wave functions is zero if the momentum transfer is in the symmetry plane.

### D. Time-, Angle-, and Energy-Resolved Ultrafast Electron Diffraction of 1-fs Electron Pulses

Although ultrafast electron diffraction of 100-fs pulses successfully images the population transfer in the lithium atom, information on the electronic motion is still incomplete. In addition to the ps-scale evolution of the population, the target state $\psi_1(t)$ actually oscillates rapidly due to the difference in the energies $\omega_{2s}$ and $\omega_{2p}$. As the valence electron is in a time-dependent coherent superposition of eigenstates having opposite parities, it wiggles from one side of the nucleus to the other with a beat period $T = 2.13$ fs. In order to map such motion, pulses with 1-fs duration (FWHM) are chosen.

The angle-resolved spectra for the 1-fs pulses are shown in the left column of Fig. 6 at time delays $t_d = 1.0$, $3.7 - T/2$, 3.7, $3.7 + T/2$, and 6.0 ps. In order to monitor the wiggling motion, the delays between the middle three panels differ by half the beat period. The azimuthal scattering angle is $\varphi = 0°$. Contrary to the 100-fs case, the spectra show continuous distributions and no channel can be clearly resolved owing to the large bandwidth of the incident electrons ($\approx 1.82$ eV). Nevertheless, the largest extension of the angular distribution is around 10 keV. Some information about the energy content of the target state can be extracted by comparing the spectra at $t_d = 1.0$ and 6.0 ps. In the energy region corresponding to the de-excitation transition ($E_a \approx 10.002$ keV) the spectrum continues to increase with delay time. The middle three panels exhibit rapid changes in the spectrum, especially on either side of the 10-keV peak. Note the similarity between the second and fourth panels, indicating that the spectrum oscillates with the same period as the electronic motion. Although it may appear that pulses with a large bandwidth have little advantage in energy-resolved measurements, we argue below that such measurements can still provide valuable insight into the interpretation of the electronic motion.

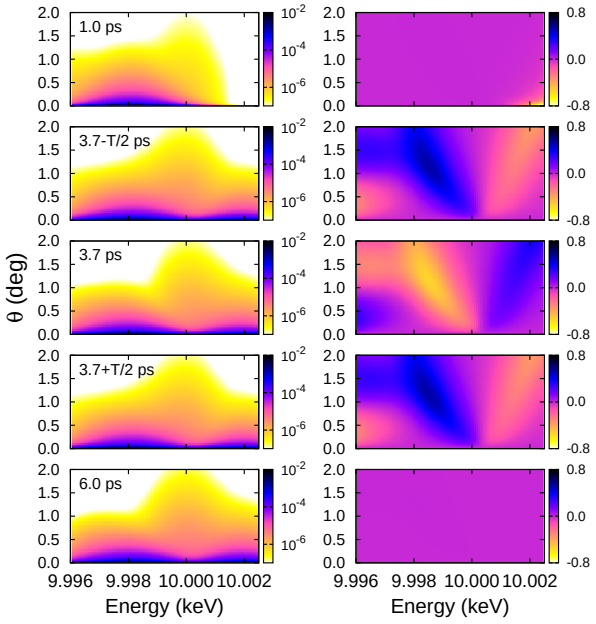


FIG. 6. (Color online) *Left column*: Ensemble-averaged doubly differential probabilities for scattering of 1-fs (FWHM) electron pulses from a $2s \to 2p$ population transfer of the valence electron in the lithium atom at five time delays: $t_d = 1.0$, $3.7 - T/2$, 3.7, $3.7 + T/2$, and 6.0 ps. The azimuthal scattering angle is $\varphi = 0°$ and the beat period between the $2s$ and $2p$ states is $T = 2.13$ fs. *Right column*: Asymmetry [defined in Eq. (46)] of the angle-resolved spectra at the corresponding time delays.

Owing to the asymmetric motion, the diffraction pattern displays an asymmetric angular distribution. In order to quantify the asymmetry, we define the *asymmetry* of the spectrum as the difference in the differential scattering probabilities for the electrons to be scattered toward positive and negative $z$ directions (*i.e.*, $\varphi = 0°$ and 180°), normalized by their sum, *i.e.*,

$$\mathrm{Asym}(E_a, \theta) \equiv \frac{d^2\mathscr{P}(\varphi = 0°) - d^2\mathscr{P}(\varphi = 180°)}{d^2\mathscr{P}(\varphi = 0°) + d^2\mathscr{P}(\varphi = 180°)}, \tag{46}$$

where $d^2\mathscr{P}$ stands for the EADDP. Nonzero asymmetry indicates the diffraction pattern breaks the centrosymmetry dictated by Friedel's law [63], and positive asymmetry means more electrons are scattered toward the positive $z$ direction. The right column of Fig. 6 shows the asymmetry of the angle-resolved spectrum as a function of delay. At $t_d = 1.0$ and 6.0 ps the asymmetry is essentially zero, since a single parity dominates the target state $\psi_1(t)$. However, when about half of the population is transferred to the $2p$ state around $t_d = 3.7$ ps, the diffraction patterns of the middle three panels show nonzero asymmetry. More importantly, the asymmetry shows an energy- and $\theta$-dependent distribution. The energy regions 9.998-10.000 keV and 10.000-10.002 keV show opposite asymmetries that are roughly mirror symmetric patterns with respect to $E_a \approx 10$ keV. Moreover, the sign of the asym-

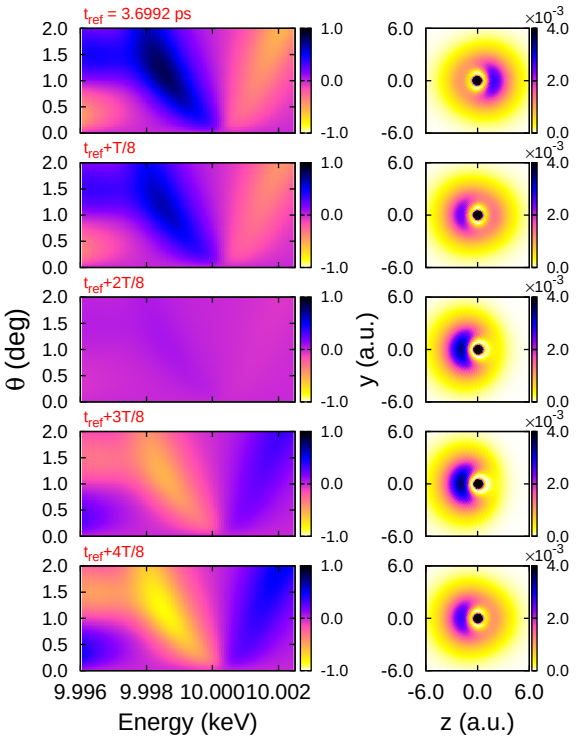


FIG. 7. (Color online) *Right column*: Time-dependent charge density of the valence electron of the lithium atom in the $y$-$z$ plane in a sequence of time intervals $T/8$. The wiggling motion starts at $t_{\rm ref} = 3.6992$ ps and extends over half the beat period $T$. *Left column*: Asymmetries [defined in Eq. (46)] of the angle-resolved scattering spectra at the corresponding time delays for the 1-fs electron pulses.

metry at lower energy ($E_a \lesssim 9.998$ keV) depends on the scattering angle $\theta$. Without energy-resolved measurements, these details in the energy-dependent diffraction pattern would not be observed in the measurements.

In order to establish the correlation between the electronic motion and the asymmetry, we compare in Fig. 7 the time-varying charge density of the valence electron in the $y$-$z$ plane with the corresponding asymmetry in a sequence of $T/8$ intervals. The series starts at $t_{\rm ref} = 3.6992$ ps and spans half the beat period. As shown in the right column of Fig. 7, the wiggling begins with the electron density localized on the right side of the core. As time elapses, the peak moves toward the negative $z$ direction, reaching the leftmost point between $t_{\rm ref}+2T/8$ and $t_{\rm ref}+3T/8$. Then the electron oscillates back toward positive $z$. The asymmetry follows the electronic motion with the asymmetry steadily evolving in time between $+1$ and $-1$ at any given point of $E_a$ and $\theta$. While the temporal behavior of the asymmetry reflects the electronic motion, the asymmetries in the density and the spectrum are not synchronized. The minimum overall asymmetry of the spectrum at $t_d = t_{\rm ref}+2T/8$ basically corresponds to the maximum asymmetry of the electron density.

This asynchrony between the temporal behavior of the diffraction spectrum and that of the charge density can be explained from the viewpoint of momentum transfer. First we focus on the asymmetry around the 10.000-10.002 keV region, in which, according to Fig. 4, the spectrum is dominated by the transitions to the $2s$ state. During the first half of the series of time delays shown in Fig. 7 the electron charge density moves toward the left, so its momentum distribution is skewed toward the negative $z$ direction whereas the momentum distribution of the final $2s$ state is symmetric with respect to the origin. Therefore, when the electron receives a momentum transfer antiparallel to its existing momentum, the target state $\psi_1(t)$ is brought toward the origin in momentum space and, hence, the shifted momentum distribution is more equally distributed with respect to the origin. Thus the overlap between the displaced target state and the $2s$ state can increase with an appropriate momentum kick. On the other hand, if the momentum transfer is parallel to the electronic motion, $\psi_1(t)$ is shifted further away from the origin and the overlap decreases accordingly. In order to yield a momentum transfer antiparallel to the electron's motion, the projectile electron has to be scattered (or recoiled) in the same direction as that of the target electron's motion. Therefore, the asymmetry in the 10.000-10.002 keV region is negative in the first half of the motion. When the electron begins to oscillate back (as shown in the last half of the series of time delays shown in Fig. 7), its momentum wave function is shifted toward the positive $z$ axis, so the asymmetry changes sign, becoming positive.

Next we turn to the asymmetry in the 9.998-10.000 keV region. As shown in Fig. 4, the main contribution in this region is the transition to the $2p$ state, whose symmetry differs from that of the $2s$ state. The $2p$ state is antisymmetric along the $z$ axis. Therefore, when the target electron receives a momentum transfer such that its wave function $\psi_1(t)$ is shifted toward the origin, the overlap between the displaced $\psi_1(t)$ and the $2p$ state can reduce the transition amplitude owing to a cancellation between the positive and negative momentum components stemming from the sign change in the $2p$ state. Therefore, in this energy region the asymmetry has the opposite sign to that in the 10.000-10.002 keV region.

## V. SUMMARY AND CONCLUSIONS

In summary, we have presented a theory to model ultrafast electron diffraction from a time-dependent population transfer driven by a chirped laser pulse. During this pump process the valence electrons of lithium atoms are transferred from the $2s$ state to the $2p$ state, and this electronic motion is imaged by energy- and angle-resolved measurements. Simulations have been performed to calculate the diffraction images as a function of time delay for electron pulses having durations of 100-fs and 1-fs. Depending on the pulse duration, different layers of information about the electronic motion can be retrieved from the energy-resolved diffraction images. In the case of 100-

fs pulses, due to its narrow bandwidth, state-resolved measurement is possible. Therefore, the time-dependent population, the time evolution of the target state symmetry, and the energy content of the target state can be deduced from a detailed analysis of different channels. In addition, the results have been interpreted from a momentum-transfer viewpoint. In the case of a 1-fs electron pulse, whereas state-resolved measurements may not be possible (*cf.* [43]), the energy-resolved diffraction images show asymmetric patterns that reflect the wiggling motion of the valence electron in the coherent superposition state of the target lithium atom. This asymmetry has been interpreted from the viewpoint of momentum transfer to the time-varying momentum distribution of the target state.

Although electronic motions in atoms are relatively simple, they nevertheless provide a stepping-stone toward understanding the more complicated electron dynamics in molecular systems. Owing to its simplicity, our system provides a testbed that enables one to understand the dynamics of ultrafast electron diffraction. Our analyses and simulations, therefore, aim to provide useful knowledge for the future development of ultrafast techniques to directly image electronic motions in complex systems.

## ACKNOWLEDGMENTS

This work was supported in part by the U.S. National Science Foundation under Grant No. PHY-1505492. This work was completed utilizing the facilities of the Holland Computing Center at the University of Nebraska.

[1] H.N. Chapman and K.A. Nugent, Coherent lensless X-ray imaging, Nat. Photon. **4**, 833 (2010).
[2] J. Miao, R.L. Sandberg, and C. Song, Coherent X-ray Diffraction Imaging, IEEE J. of Selected Topics in Quantum Electronics **18**, 399 (2012).
[3] A. Barty, J. Küpper, and H.N. Chapman, Molecular Imaging Using X-Ray Free-Electron Lasers, Annu. Rev. Phys. Chem. **64**, 415 (2013).
[4] J. Miao, T. Ishikawa, I.K. Robinson, and M.M. Murnane, Beyond crystallography: Diffractive imaging using coherent x-ray light sources, Science **348**, 530 (2015).
[5] E.O. Wollan, X-Ray Scattering and Atomic Structure, Rev. Mod. Phys. **4**, 205 (1932).
[6] R. A. Bonham and M. Fink, *High Energy Electron Scattering* (Van Nostrand Reinhold, New York, 1974).
[7] N. Jones, Crystallography: Atomic secrets, Nature **505**, 602-603 (30 January 2014). doi:10.1038/505602a
[8] G. Sciaini and R.J.D. Miller, Femtosecond electron diffraction: heralding the era of atomically resolved dynamics, Rep. Prog. Phys. **74**, 096101 (2011).
[9] S. Corde, K. Ta Phuoc, G. Lambert, R. Fitour, V. Malka, A. Rousse, A. Beck, and E. Lefebvre, Femtosecond x rays from laser-plasma accelerators, Rev. Mod. Phys. **85**, 1 (2013).
[10] C. Bostedt, S. Boutet, D.M. Fritz, Z. Huang, H.J. Lee, H.T. Lemke, A. Robert, W.F. Schlotter, J.J. Turner, and G.J. Williams, Linac Coherent Light Source: The first five years, Rev. Mod. Phys. **88**, 015007 (2016).
[11] P. Baum and F. Krausz, Capturing atomic-scale carrier dynamics with electrons, Chem. Phys. Lett. **683**, 57 (2017).
[12] R.J.D. Miller, Femtosecond Crystallography with Ultrabright Electrons and X-rays: Capturing Chemistry in Action, Science **343**, 1108 (2014).
[13] A.H. Zewail, 4D Ultrafast Electron Diffraction, Crystallography, and Microscopy, Annu. Rev. Phys. Chem. **57**, 65 (2006).
[14] A.H. Zewail, Four-Dimensional Electron Microscopy, Science **328**, 187 (2010).
[15] J.M. Thomas, R.K. Leary, A.S. Eggeman, and P.A. Midgley, The rapidly changing face of electron microscopy, Chem. Phys. Lett. **631-632**, 103 (2015). http://dx.doi.org/10.1016/j.cplett.2015.04.048
[16] M. Centurion, Topical Review: Ultrafast imaging of isolated molecules with electron diffraction, J. Phys. B **49**, 062002 (2016).
[17] R.J.D. Miller, Ultrafast imaging of photochemical dynamics: roadmap to a new conceptual basis for chemistry, Faraday Discuss. **194**, 777 (2016).
[18] H. Ihee, V.A. Lobastov, U.M. Gomez, B.M. Goodson, R. Srinivasan, C.-Y. Ruan, and A.H. Zewail, Direct Imaging of Transient Molecular Structures with Ultrafast Diffraction, Science **291**, 458 (2001).
[19] J. Yang, J. Beck, C.J. Uiterwaal, and M. Centurion, Imaging of alignment and structural changes of carbon disulfide molecules using ultrafast electron diffraction, Nat. Commun. **6**, 8172 (2015).
[20] J. Yang *et al.*, Diffractive Imaging of Coherent Nuclear Motion in Isolated Molecules, Phys. Rev. Lett. **117**, 153002 (2016).
[21] M. Gao *et al.*, Mapping molecular motions leading to charge delocalization with ultrabright electrons, Nature **496**, 343 (2013).
[22] T. Ishikawa *et al.*, Direct observation of collective modes coupled to molecular orbital-driven charge transfer, Science **350**, 1501 (2015).
[23] B.-K. Yoo, O.-H. Kwon, H. Liu, J. Tang, and A.H. Zewail, Observing in space and time the ephemeral nucleation of liquid-to-crystal phase transitions, Nat. Commun. **6**, 8639 (2015).
[24] V.R. Morrison, R.P. Chatelain, K.L. Tiwari, A. Hendaoui, A. Bruhács, M. Chaker, and B.J. Siwick, A photoinduced metal-like phase of monoclinic $VO_2$ revealed by ultrafast electron diffraction, Science **346**, 445 (2014).
[25] L. Waldecker, T.A. Miller, M. Rudé, R. Bertoni, J. Osmond, V. Pruneri, R.E. Simpson, R. Ernstorfer, and S. Wall, Time-domain separation of optical properties from structural transitions in resonantly bonded materials, Nat. Mater. **14**, 991 (2015).
[26] A. Ryabov and P. Baum, Electron microscopy of electromagnetic waveforms, Science **353**, 374 (2016).
[27] J. Hoffrogge, J.P. Stein, M. Krüger, M. Förster, J. Hammer, D. Ehberger, P. Baum, and P. Hommelhoff, Tip-based source of femtosecond electron pulses at 30 keV, J.

Appl. Phys. **115**, 094506 (2014).
[28] L. Waldecker, R. Bertoni, and R. Ernstorfer, Compact femtosecond electron diffractometer with 100 keV electron bunches approaching the single-electron pulse duration limit, J. Appl. Phys. **117**, 044903 (2015).
[29] C. Gerbig, A. Senftleben, S. Morgenstern, C. Sarpe, and T. Baumert, Spatio-temporal resolution studies on a highly compact ultrafast electron diffractometer, New J. Phys. **17**, 043050 (2015).
[30] P. Zhu *et al.*, Femtosecond time-resolved MeV electron diffraction, New J. Phys. **17**, 063004 (2015).
[31] A. Gliserin, M. Walbran, F. Krausz, P. Baum, Sub-phonon-period compression of electron pulses for atomic diffraction, Nat. Commum. **6**, 8723 (2015).
[32] J. Maxson, D. Cesar, G. Calmasini, A. Ody, P. Musumeci, and D. Alesini, Direct Measurement of Sub-10 fs Relativistic Electron Beams with Ultralow Emittance, Phys. Rev. Lett. **118**, 154802 (2017).
[33] A. Gliserin, A. Apolonski, F. Krausz, and P. Baum, Compression of single-electron pulses with a microwave cavity, New J. Phys. **14**, 073055 (2012).
[34] P. Hansen, C. Baumgarten, H. Batelaan, and M. Centurion, Dispersion compensation for attosecond electron pulses, Appl. Phys. Lett. **101**, 083501 (2012).
[35] L.J. Wong, B. Freelon, T. Rohwer, N. Gedik, and S.G. Johnson, All-optical three-dimensional electron pulse compression, New. J. Phys. **17**, 013051 (2015).
[36] S.R. Greig and A.Y. Elezzabi, Generation of attosecond electron packets via conical surface plasmon electron acceleration, Sci. Rep. **6**, 19056 (2016).
[37] F.C. Vélez, J.Z. Kamiński, and K. Krajewska, Generation of attosecond electron beams in relativistic ionization by short laser pulses, arXiv:1702.03499 [physics.atom-ph]
[38] K. Krajewska, F.C. Velez, and J.Z. Kamiński, Generation of attosecond electron pulses using petawatt lasers, Proc. SPIE **10241**, 102411J (2017). doi: 10.1117/12.2271138
[39] S. Tanaka, V. Chernyak, and S. Mukamel, Time-resolved x-ray spectroscopies: Nonlinear response functions and Liouville-space pathways, Phys. Rev. A **63**, 03405 (2001).
[40] P. Baum, J. Manz, and A. Schild, Quantum model simulations of attosecond electron diffraction, Sci. China Phys. Mech. Astron. **53**, 987 (2010).
[41] G. Dixit, O. Vendrell, and R. Santra, Imaging electronic quantum motion with light, Proc. Natl. Acad. Sci. USA **109**, 11636 (2012).
[42] H.-C. Shao and A.F. Starace, Imaging coherent electronic motion in atoms by ultrafast electron diffraction, Phys. Rev. A **88**, 062711 (2013).
[43] H.-C. Shao and A.F. Starace, Imaging electronic motions in atoms by energy-resolved ultrafast electron diffraction, Phys. Rev. A **90**, 032710 (2014).
[44] M. Grosser, J.M. Slowik, and R. Santra, Attosecond x-ray scattering from a particle-hole wave packet, Phys. Rev. A **95**, 062107 (2017).
[45] H.-C. Shao and A.F. Starace, Imaging population transfer in atoms with ultrafast electron pulses, Phys. Rev. A **94**, 030702(R) (2016).
[46] J.S. Melinger, S.R. Gandhi, A. Hariharan, D. Goswami, and W.S. Warren, Adiabatic population transfer with frequency-swept laser pulses, J. Chem. Phys. **101**, 6439 (1994).
[47] N.V. Vitanov, T. Halfmann, B.W. Shore, and K. Bergmann, Laser-Induced Population Transfer by Adiabatic Passage Techniques, Annu. Rev. Phys. Chem. **52**, 763 (2001).
[48] K. Bennett, J.D. Biggs, Y. Zhang, K.E. Dorfman, and S. Mukamel, Time-, frequency-, and wavevector-resolved x-ray diffraction from single molecules, J. Chem. Phys. **140**, 204311 (2014).
[49] P. Francken and C.J. Joachain, Theoretical study of electron-atom collisions in intense laser fields, J. Opt. Soc. Am. B **7**, 554 (1990).
[50] M. Dörr, C.J. Joachain, R.M. Potvliege, and S. Vučić, Born-Floquet theory of laser-assisted electron-atom collisions, Phys. Rev. A **49**, 4852 (1994).
[51] F. Eholtzky, A. Jaroń, and J.Z. Kamiński, Electron-atom collisions in a laser field, Phys. Rep. **297**, 63 (1998).
[52] V.P. Krainov, H.R. Reiss, and B.M. Smirnov, *Radiative Processes in Atomic Physics* (John Wiley & Sons, Inc., New York, 1997).
[53] R.G. Newton, *Scattering Theory of Waves and Particles, 2nd ed.* (Dover, Inc., New York, 2002).
[54] C.J. Joachain, N.J. Kylstra, and R.M. Potvliege, *Atoms in Intense Laser Fields* (Cambridge University Press, Cambridge, U.K., 2012), Sec. 2.2.
[55] H. A. Bethe and R. W. Jackiw, *Intermediate Quantum Mechanics, 2nd ed.* (W. A. Benjamin, New York, 1968).
[56] D.V. Karlovets, G.L. Kotkin, V.G. Serbo, and A. Surzhykov, Scattering of twisted electron wave packets by atoms in the Born approximation, Phys. Rev. A **95**, 032703 (2017).
[57] M.E. Peskin and D.V. Schroeder, *An Introduction to Quantum Field Theory* (Addision-Wesley, Reading, MA, 1995).
[58] F. Herman and S. Skillman, *Atomic Structure Calculations* (Prentice-Hall, Inc., Englewood Cliffs, New Jersey, 1963).
[59] W.I. McAlexander, E.R.I. Abraham, and R.G. Hulet, Radiative lifetime of the 2P state of lithium, Phys. Rev. A **54**, R5 (1996).
[60] K. Krajewska and J.Z. Kamiński, Supercontinuum in ionization by relativistically intense and short laser pulses: Ionization without interference and its time analysis, Phys. Rev. A **94**, 013402 (2016).
[61] J. Gillot, A. Gauguet, M. Büchner, and J. Vigué, Optical pumping of a lithium atomic beam for atom interferometry, Eur. Phys. J. D **67**, 263 (2013).
[62] P. Baum and A.H. Zewail, Breaking resolution limits in ultrafast electron diffraction and microscopy, Proc. Natl. Acad. Sci. USA **103**, 16105 (2006).
[63] G. Friedel, Sur les symétries cristallines que peut révéler la diffraction des rayons Röntgen, Comptes Rendus Acad. Sci. **157**, 1533 (1913).